



# Multiscale seismic attributes: a wavelet-based method and its application to high-resolution seismic and ground truth data

Stephan Ker, Yves Le Gonidec, Dominique Gibert, Bruno Marsset

## ► To cite this version:

Stephan Ker, Yves Le Gonidec, Dominique Gibert, Bruno Marsset. Multiscale seismic attributes: a wavelet-based method and its application to high-resolution seismic and ground truth data. *Geophysical Journal International*, 2011, 187 (2), pp.1038-1054. 10.1111/j.1365-246X.2011.05207.x . insu-00669844

**HAL Id: insu-00669844**

**<https://insu.hal.science/insu-00669844>**

Submitted on 18 May 2017

**HAL** is a multi-disciplinary open access archive for the deposit and dissemination of scientific research documents, whether they are published or not. The documents may come from teaching and research institutions in France or abroad, or from public or private research centers.

L'archive ouverte pluridisciplinaire **HAL**, est destinée au dépôt et à la diffusion de documents scientifiques de niveau recherche, publiés ou non, émanant des établissements d'enseignement et de recherche français ou étrangers, des laboratoires publics ou privés.

# Multiscale seismic attributes: a wavelet-based method and its application to high-resolution seismic and ground truth data

S. Ker,<sup>1,2</sup> Y. Le Gonidec,<sup>3</sup> D. Gibert<sup>2</sup> and B. Marsset<sup>1</sup>

<sup>1</sup>Département Géosciences Marines, IFREMER, Centre de Brest, 29280 Plouzané, France. E-mail: stephan.ker@ifremer.fr

<sup>2</sup>Institut de Physique du Globe de Paris (CNRS UMR 7154), Sorbonne Paris Cité, 1 rue Jussieu, 75238 Paris cedex, France

<sup>3</sup>Géosciences Rennes (CNRS UMR 6118), Université Rennes 1, Bât. 15 Campus de Beaulieu, 35042 Rennes cedex, France

Accepted 2011 August 26. Received 2011 June 8; in original form 2011 February 22

## SUMMARY

We propose a wavelet-based method to characterize acoustic impedance discontinuities from a multiscale analysis of seismic reflected waves. Our approach relies on the analysis of ridge functions which contain most of the information of the wavelet transform in a sparse support. This method falls in the framework of the wavelet response (WR) introduced by Le Gonidec *et al.* which analyses the impedance multiscale behaviour by propagating dilated wavelets into the medium. We further extend the WR by considering its application to broad-band seismic data. We take into account the bandpass filter effect related to the limited frequency range of the seismic source. We apply the method to a deep-water seismic experiment performed in 2008 during the ERIG3D cruise to demonstrate the potential of ridge functions as multiscale seismic attributes. In conjunction to the analysis of seismic data acquired by the deep-towed SYSIF system (200–2200 Hz), we use ground truth data to characterize the fine scale structure of superficial sediments by using the continuous wavelet transform (CWT). The availability of *in situ* measurements allows to validate the relationship between CWT and WR and to estimate the attenuation of seismic waves into the sediments. Once validated, the method is applied on a whole seismic profile and WR ridge functions are computed for two particular reflectors. The reflector thicknesses fall below the resolution limit of the seismic experiment making the WR seismic attributes a super-resolution method.

**Key words:** Wavelet transform; Seismic attenuation; Wave propagation; Acoustic properties.

## 1 INTRODUCTION

The characterization of both petrological and mechanical properties of marine sediments in large areas often relies on the joined analysis of both seismic survey data and local ground truth measurements obtained from wells and cores (e.g. Sheriff 1992; Pennington 2001; Sultan *et al.* 2007a). This kind of approach falls in the main topic of applied seismology where a quantitative mutual analysis of seismic soundings and *in situ* data is performed to derive links between seismic attributes and properties of the geological medium (Barnes 2001; Fomel 2007). Many of these studies rely on statistically established relationships between seismic features and geological properties (e.g. Gastaldi *et al.* 1997). Because of the variety of attributes and the diversity of the geological properties to be determined, seismic interpreters are faced with a huge combinatorial complexity for which data mining and non-linear search algorithms are involved (e.g. Banchs & Michelena 2002; Strecker & Uden 2002).

A notable difficulty encountered when relating seismic attributes and core data comes from the generally huge discrepancy existing between the frequency range of the high-resolution (HR) *in situ* data and the low-frequency range of the filtered seismic traces (Widess

1973; Banik *et al.* 1985; Burridge *et al.* 1988). Consequently, the seismic data furnish a blurred, low-pass filtered view of the geological interfaces producing the reflected waves. This prohibits a simple correspondence between seismic arrivals and reflectors. In particular, a small-scale cluster of geological interfaces may appear as a single equivalent seismic reflector either because of the intrinsic low-frequency nature of the incident waves (Marsset *et al.* 2010) or because of low-pass filtering effects produced by interferences occurring within the cluster of interfaces (e.g. Morlet *et al.* 1982). These effects are often reinforced and complicated by the conjugation of multiple scattering produced by small-scale heterogeneities (Banik *et al.* 1985; Resnick 1990) and the fractal nature of the heterogeneous geological layers (Frankel & Clayton 1986; Sheng *et al.* 1986). However, the degradation of the resolution produced by these filtering phenomena constitutes, by itself, an information which provides constraints on the properties of the complex heterogeneous geological medium (Aki & Chouet 1975; Le Gonidec & Gibert 2007).

Considerable efforts are being made to widen the frequency range of seismic apparatus by pushing the limits due to technological constraints, especially the physical properties of the seismic

sources which mainly radiate their energy in the low-frequency domain (Gettrust *et al.* 1991; Wood *et al.* 2003; Marsset *et al.* 2010). Important technological advances have recently been obtained for full deep-towed devices, equipped with both sources and receivers, allowing to perform measurements close to the seafloor. Such new seismic tools, like the SYSIF seismic device developed by IFREMER (Ker *et al.* 2008; Ker *et al.* 2010; Marsset *et al.* 2010), furnish a better penetration of the seismic waves into the sediments and a dramatic improvement of the frequency content of the seismic data.

The significant widening of the available frequency range motivates further developments in the local analysis of seismic traces. Indeed, active research on seismic attributes gained a renewal of interest during the last decade to propose new seismic attributes and study their relation with yet seismically unrecognized geologic features (e.g. Chopra & Marfurt 2008). In particular, the wide frequency range of the data now available allows to undertake spectral decompositions in the seismic attribute domain to obtain information on the fine structure of the reflectors (Chopra & Marfurt 2008). In the most recent studies, time-frequency decomposition, using either windowed Fourier transform or continuous wavelet analysis, to perform a local spectral decomposition of seismic arrivals (Castagna *et al.* 2003; Chopra *et al.* 2006). These promising new approaches transfer the information originally contained in the seismic traces into multidimensional spaces where the time-frequency characteristics of the reflected wave packets are used to derive information about the nature of the reflectors.

The aim of this paper is to contribute to the understanding of the wavelet decomposition of seismic traces by exploiting the physical phenomena—interferences, attenuation—influencing the wavelet transform signature of seismic wave packets. Here, the wavelets must be understood in the sense of the constant shape wavelets used in wavelet analysis (e.g. Goupillaud *et al.* 1984). Our approach relies on the analysis of the so-called ridge functions formed by lines of extrema in the wavelet transform (Mallat & Hwang 1992; Alexandrescu *et al.* 1995; Mallat 1998; Le Gonidec *et al.* 2002). As explained later in this paper, such lines constitute a sparse support containing much of the information brought by the wavelet transform. Indeed, Mallat & Hwang (1992) showed that, under some conditions, a complex signal may be reconstructed with the sole ridge function skeleton extracted from its wavelet transform.

We propose to consider the ridge functions extracted from wavelet transforms of seismic traces as seismic attributes. In Section 2, we show how the ridge functions of the wavelet transform of the seismic data may provide information on the small-scale structure of the reflectors. Our work falls in the framework of the wavelet response (WR) introduced by Le Gonidec *et al.* (2002), and defined as the seismic traces obtained for a family of source signals corresponding to wavelets with different dilations. These authors showed that the ridge functions of the WR contain informations on the shape of the impedance variations—not necessarily step-like jumps—associated with the reflectors (Le Gonidec *et al.* 2002; Le Gonidec & Gibert 2006, 2007; Gesret *et al.* 2010).

In this paper, we further extend the WR approach by considering the application of the method to real seismic data. In particular, we study the distortions produced by the limited frequency range of the source used in real seismic surveys. To illustrate the potential usefulness of the seismic attributes constituted by the ridge functions, we apply them to a deep-water seismic experiment performed in year 2008 during the ERIG3D cruise (Ker *et al.* 2010), and where HR seismic measurements were done in two frequency bands (220–1050 Hz) and (580–2200 Hz) to obtain very high reso-

lution (VHR) seismic images of the superficial sediment structures (Fig. 1). In conjunction to these original seismic data, ground truth data—both penetrometer and core measurements—are used to characterize the fine structure of the layered geological medium at some locations along a seismic profile.

The paper is organized as follows. Section 2 introduces the theoretical framework of the multiscale analysis illustrated on theoretical discontinuities, that is, reflectors with simple geometries. Section 3 is devoted to ground truth data constituted by a sediment core and *in situ* measurements (density and *P*-wave velocity). We describe the processing and corrections applied to obtain the acoustic impedance log of the site that we used to perform the multiscale analysis of the superficial marine sediments. In Section 4, we consider the deep-towed SYSIF seismic data and compare their WR with the wavelet transform of the impedance log. Afterwards, the entire seismic profile is processed and ridge function seismic attributes are used to follow the along-profile variations of the characteristic thickness of reflectors.

## 2 WAVELET-BASED MULTISCALE ANALYSIS OF COMPLEX DISCONTINUITIES

This section presents a multiscale analysis of complex discontinuities based on the continuous wavelet transform (CWT). We first recall the main properties of the CWT to characterize discontinuities present in vertical profiles of the acoustic impedance as measured in boreholes. We next examine how the CWT analysis can be extended to the WR analysis to detect and characterize impedance discontinuities by using the reflected waves instead of the impedance profile. Finally, we address the case of real seismic data with finite frequency bandwidth that do not allow to obtain a pure WR, and for which distortions occur.

### 2.1 Multiscale analysis in the space domain: the continuous wavelet transform

This section contains the fundamental properties of the CWT to detect and characterize discontinuities present in signals corresponding to vertical profiles  $p(z)$  of either density, *P*-wave velocity or acoustic impedance. Such discontinuities produce reflection and refraction of incident waves and correspond to seismic reflectors. We consider the case of complex impedance variations representable as a sum of a finite number of elementary singularities sharing the common homogeneity property

$$\mathcal{D}_a p(z) \equiv \frac{1}{a} p\left(\frac{z}{a}\right) = \left(\frac{1}{a}\right)^{\alpha+1} p(z), \quad (1)$$

where  $\alpha$  is the homogeneity degree which depends on the type of singularity (Holschneider 1995) and  $\mathcal{D}_a$  is a dilation operator (Goupillaud *et al.* 1984) with  $a > 0$ , the dilation parameter also referred to as the scale factor. The CWT of  $p(z)$  is defined as

$$W[\psi, p](z, a) \equiv (\mathcal{D}_a \psi * p)(z) \quad (2a)$$

$$= \frac{1}{a} \psi\left(\frac{z}{a}\right) * p(z), \quad (2b)$$

where  $*$  denotes the convolution operator.  $\psi$  is a given function called the mother-analysing wavelet, where wavelength is  $\lambda_0$ . The factor  $a$  is defined as  $a = \lambda/\lambda_0$  where  $\lambda$  is the wavelength of the dilated wavelet. Indeed, for functions  $p$

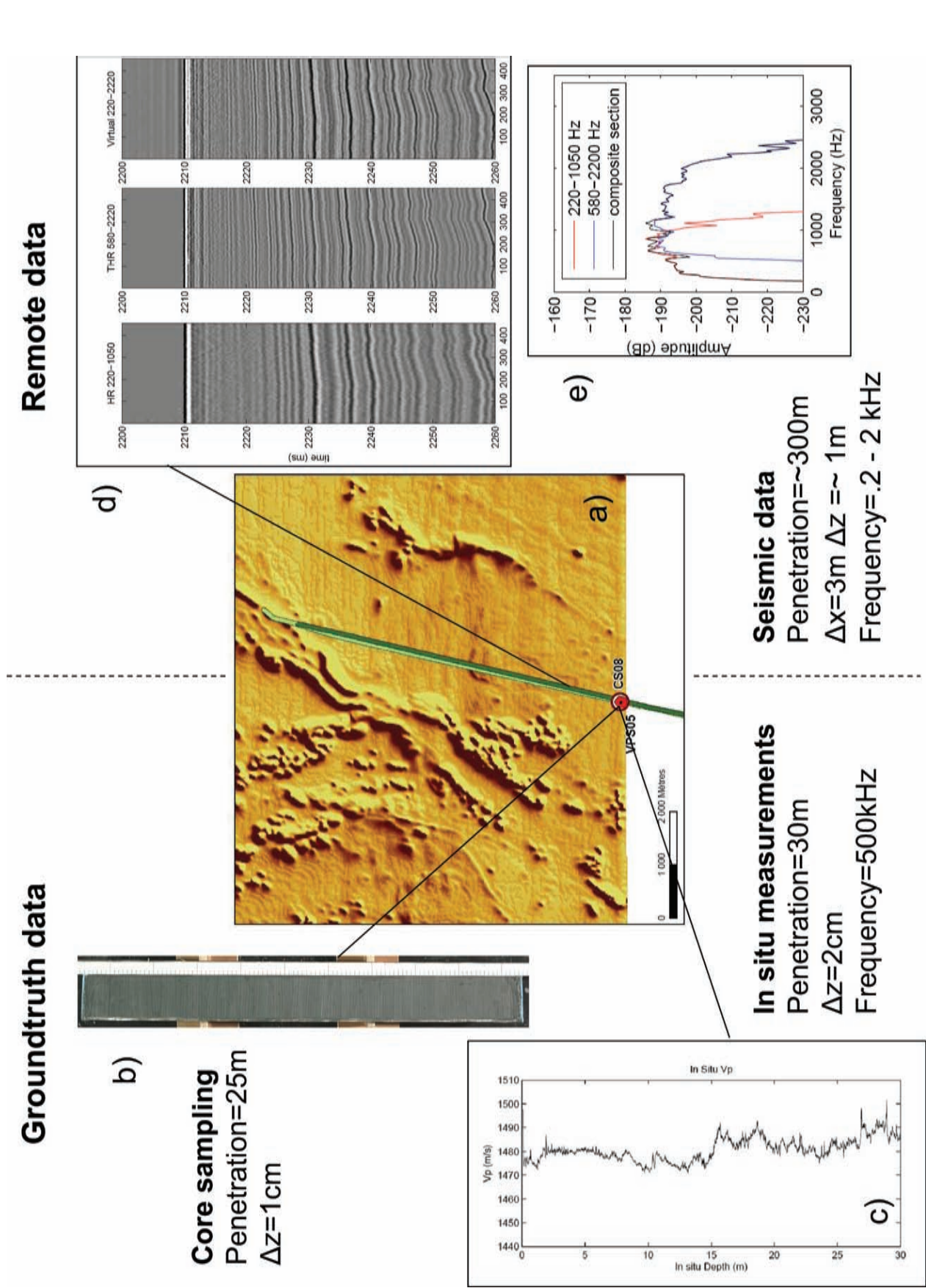


**Figure 1.** (a) Location of the seismic profile and ground truth data acquired during the ERIG3D cruise. (b) Photograph of the CS-08 core. (c) *In situ* P-wave velocity log. (d) Seismic profiles at the coring site, with a high-resolution [HR: (220–1050 Hz)], very high resolution [VHR: (580–2200 Hz)] and a combination of both. (e) Frequency spectra of the HR, VHR and composite seismic profiles.

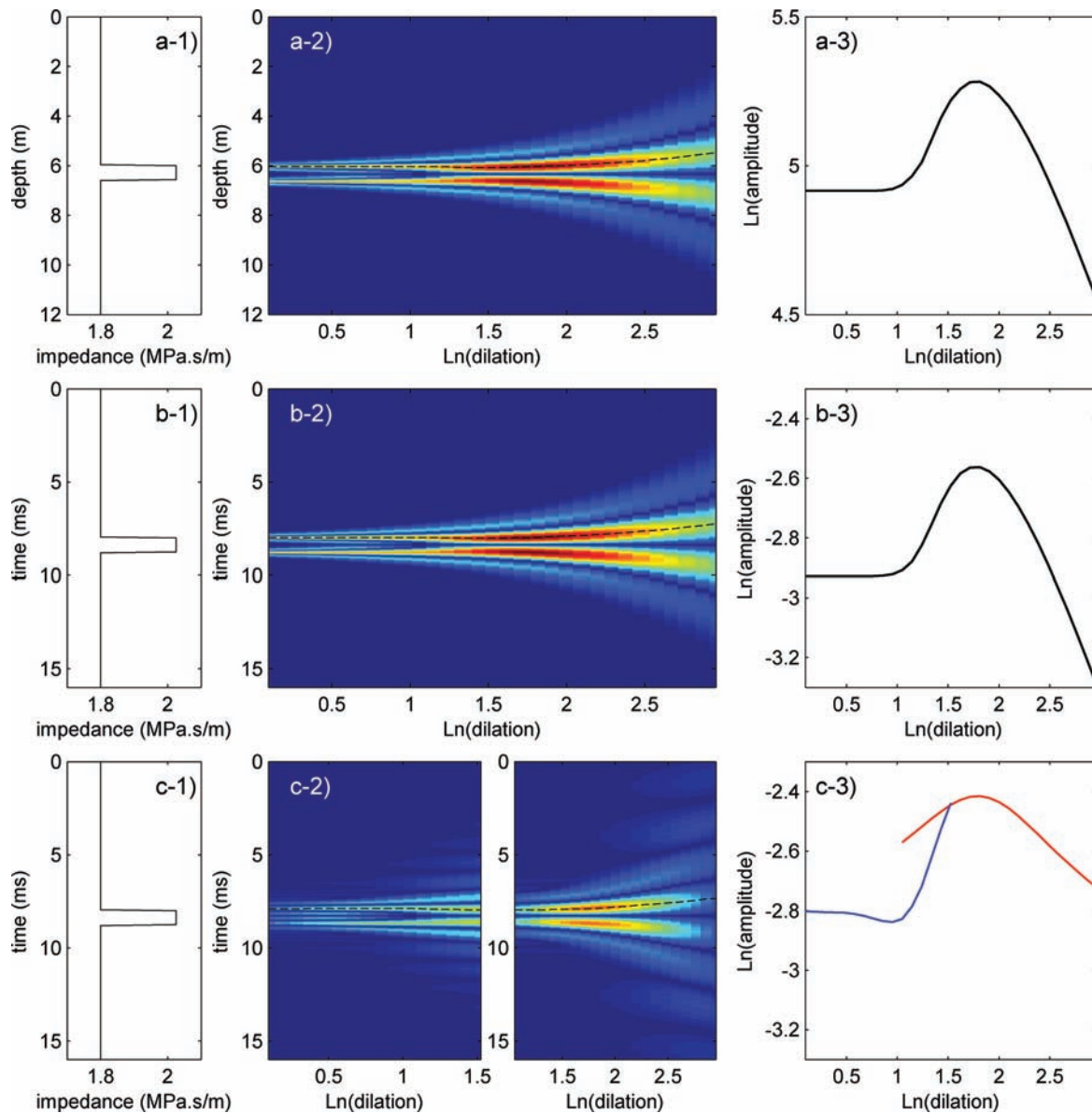


**Figure 2.** Top panels (left- to right-hand side): complex discontinuity of aperture  $\Delta z = 0.6$  m and modulus of the wavelet transform (WT) in the depth-dilation domain and ridge function. Middle panels (left- to right-hand side): complex discontinuity and modulus of the wavelet response (WR) in the time-dilation domain and ridge function. Bottom panels (left- to right-hand side): complex discontinuity, WR modulus in two dilation ranges including band-limited distortions and ridge function (log is the neperian logarithm).

satisfying eq. (1), we have

$$W[\psi, p](z, a') = \left(\frac{a'}{a}\right)^{\alpha+1} \mathcal{D}_{a'/a} W[\psi, p](z, a). \quad (3)$$

Eq. (3) states that the entire CWT of a homogeneous singularity can be recovered from its values taken at a single dilation  $a$  (Grossmann *et al.* 1987; Holschneider 1988; Mallat & Hwang 1992). Geometrically, eq. (3) indicates that the wavelet transform of an isolated homogeneous singularity has a cone-like appearance with the apex pointing onto the singularity location. The analysing wavelet  $\psi$  may be any localized oscillating function with a vanishing integral; however, it must also have at least  $\alpha$  vanishing moments to preserve the localized conical shape of the wavelet transform of a singularity with homogeneity degree  $\alpha$ . In this work,  $\psi$  is taken as the third derivative of a Gaussian function and possesses four extrema.

Eq. (3) also shows that the amplitude of the CWT of a homogeneous singularity scales as  $a^\alpha$ . By plotting the absolute value of the CWT taken along its lines of extrema as a function of  $a$ , straight lines with slope  $\alpha$  in a log-log diagram characterize the singularity geometry (Mallat & Hwang 1992; Alexandrescu *et al.* 1995; Holschneider 1995; Moreau *et al.* 1997; Le Gonidec *et al.* 2002). In Appendix A, we remember the basic results for two ideal discontinuities, that is, the Dirac and the Heaviside functions.

When combining such homogeneous singularities, the resulting complex discontinuities will no more be homogeneous and, consequently, they will have one or more characteristic scales. We shall suppose that the centres of homogeneity of these singularities are contained in an interval of finite width. As an example, let us consider a window discontinuity,  $w$ , constructed with two Heaviside functions  $H$  ( $\alpha = 0$ ) of opposite signs and separated by  $\Delta z$  (Fig. 2a-1),

$$w(z) = H\left(z + \frac{\Delta z}{2}\right) - H\left(z - \frac{\Delta z}{2}\right). \quad (4)$$

Invoking the linearity of the wavelet transform and using eq. (3), we get

$$W[\psi, w](z, a) = W[\psi, H]\left(z + \frac{\Delta z}{2}, a\right) - W[\psi, H]\left(z - \frac{\Delta z}{2}, a\right) \quad (5a)$$

$$= W[\psi, H]\left(\frac{z + \frac{\Delta z}{2}}{a}, 1\right) - W[\psi, H]\left(\frac{z - \frac{\Delta z}{2}}{a}, 1\right). \quad (5b)$$

As can be observed on Fig. 2(a-2), at small enough dilations (i.e. scales) the compact supports of the wavelet transforms of the two-step discontinuities forming  $w$  are disjoint and the window discontinuity appears as two distinct step discontinuities. Conversely, when  $a \rightarrow +\infty$ , eq. (5b) becomes

$$W[\psi, w](z, a) = \frac{\Delta z}{2a} \frac{d}{d(z/a)} W[\psi, H]\left(\frac{z}{a}, 1\right), \quad (6)$$

and the window of finite width  $\Delta z$  is seen as a Dirac discontinuity (Fig. 2a-2). These asymptotic appearances of the window discontinuity are also visible in the lines of extrema hereafter called ridge functions whose slope  $\alpha = 0$  at small dilations and  $\alpha = -1$  for large ones (Fig. 2a-3). Observe that the number of ridge functions in Fig. 2(a-2) changes accordingly, with two groups of three ridges typical of step discontinuities at small scales (internal structure of  $w$ ) and a single group of four ridges typical of an impulse discontinuity at large scales (global structure of  $w$ ). See Appendix A for a quantitative description of the transition between these two behaviours. At intermediate dilations, corresponding to a complicated appearance of the CWT which can no more be discussed in term of homogeneous discontinuities, the ridge functions are not straight but curved lines whose precise shape depends on the structure of the complex discontinuity. Consequently, the intermediate dilation range contains much informations relevant to the internal morphological characteristics of the discontinuity. Actually, the ridge functions of the window discontinuity possess a maximum located at the critical dilation  $a_c$  whose value is related to the characteristic size  $\Delta z$  of the window function.

In this case of Fig. 2(a), where we fixed  $\Delta z = 0.6$  m and the reference wavelength  $\lambda_0 = 0.26$  m for the mother-analysing wavelet, we get  $a_c \simeq 6.05$  [ $\ln(a_c) \simeq 1.8$ ] and

$$\lambda_c = a_c \lambda_0 \simeq 2.61 \Delta z. \quad (7)$$

The proportionality factor 2.61, specific to the considered analysing wavelet, was already introduced in Kallweit & Wood (1982) and Chung & Lawton (1995) for Ricker signals. The knowledge of  $a_c$ , measured from the ridge functions with an uncertainty  $\delta a$ , allows the determination of the thickness  $\Delta z$  with an error of  $\pm 1$  cm.

The example of the CWT analysis of the window discontinuity illustrates the general capability of CWT to perform a morphological multiscale analysis of complex intricate discontinuities from the appearance of both the CWT map and its ridge functions. The main properties of the wavelet transform discussed in this example—that is, asymptotic behaviour, intermediate dilations and merging of ridge functions—are retrieved for more complex discontinuities, provided the spanned dilation range is sufficiently large. However, the complexity of the analysed discontinuities may preclude full analytical developments like those made in Appendix A for the

window discontinuity. In such cases, a numerical inverse approach should be used instead as will be described in a forthcoming paper.

## 2.2 Multiscale analysis in the time domain: the wavelet response

We now turn to the problem of characterizing impedance discontinuities—that is, reflectors—not directly from the impedance vertical profile,  $p(z)$ , as performed in the preceding section but, instead, by analysing the waves reflected by the geological medium whose structure corresponds to the impedance profile of interest. This is accomplished by replacing the CWT described in the preceding section by the WR introduced by Le Gonidec *et al.* (2002). Instead of convolving a family of dilated wavelets with  $p(z)$  as in the CWT (see eq. 2b), the WR is obtained by propagating a wavelet family through a medium whose impedance profile corresponds to  $p(z)$ . Accordingly, the WR is defined as

$$R[\xi, p](t, a) \equiv (\mathcal{D}_a \xi \otimes p)(t) \quad (8a)$$

$$= \mathcal{D}_a \xi(t) * r(t), \quad (8b)$$

where  $\otimes$  represents the 1-D propagation of the dilated wavelet  $\mathcal{D}_a \xi(t)$  through the medium. The function  $r(t)$  is the Green's function of the medium, also known as the reflectivity function. Using  $r(t)$  instead of  $p(z)$  allows to write the WR as a convolution product. Physically, the WR represents the collection of the reflected time-varying wavefields obtained by exciting the medium with a family of dilated source wavelets. A notable difference is that the depth  $z$  axis of the CWT is now replaced by the two-way traveltime  $t$  axis in the WR.

Le Gonidec *et al.* (2002, 2003) have shown that, provided the Born approximation is valid, the WR and the CWT of homogeneous discontinuities are equivalent, that is, they produce the same ridge function and eq. (7) remains valid. In other words, the WR obtained with the reflected waves provides the same information on the singularities as if a CWT was directly applied on the impedance profile. This is illustrated in Fig. 2(b) where a window discontinuity in the impedance profile (Fig. 2b-1) produces a WR (Fig. 2b-2) similar to the wavelet transform of the window (Fig. 2a-2) with similar ridge functions (Fig. 2b-3). To obtain a full equivalence between the CWT and the WR, the latter is computed for source wavelets,  $\mathcal{D}_a \xi(t)$  equal to the integrals of the wavelets,  $\mathcal{D}_a \psi(z)$ , used to computed the CWT, that is,  $\psi = \xi'$ . In particular, the WR of a step discontinuity reproduces the source wavelets whereas the CWT gives the integrated wavelets (see Le Gonidec *et al.* 2002, 2003 and Appendix B for more details). This derivative relationship between the families of wavelets used to compute  $R$  (eq. 8b) and  $W$  (eq. 2b) allows to apply the results of the CWT to the WR methods, which involve, in this work, a third and a second Gaussian derivatives, respectively. Note that the second Gaussian derivative is the Ricker wavelet commonly used in seismic modelling.

## 2.3 Wavelet response with band-limited seismic data

Up to now, we introduced the theoretical framework of both the CWT and the WR without any consideration of limitation on the dilation range spanned by these methods. Actually, excepted in experiments where high-frequency devices can be operated to obtain WR spanning up to six octaves in the dilation domain (Le Gonidec & Gibert 2006, 2007), most seismic data have a limited bandwidth (Parkes & Hatton 1986; Sheriff 1991). We now extend the WR

to analyse such seismic data instead of assuming ideal unlimited frequency contents. This puts limits on the dilation range practically attainable and alters the scale resolution. In this section, we address some practical consequences of these limitations.

As seen in the examples concerning both the CWT and the WR, much information concerning the internal morphological structure of a complex discontinuity is contained in the high- and intermediate-dilation domains where the wavelength of the wavelets is on the order of the characteristic scales of the features forming the discontinuity. Consequently, much limitation of the performances of the WR mainly comes from the high-frequency cut-off in the data spectrum, and less from the low-frequency limit. In the discussion below, we shall assume that the limitation of the frequency bandwidth of the seismic data may be represented by a single bandpass filter with an impulse response  $b(t)$ . In such a case, eq. (8b) becomes

$$R[\xi, p](t, a) \equiv \mathcal{D}_a \xi(t) * [r(t) * b(t)] \quad (9a)$$

$$= [\mathcal{D}_a \xi(t) * b(t)] * r(t) \quad (9b)$$

$$= W[\xi, b](t, a) * r(t), \quad (9c)$$

where, owing to the associative property of the convolution product, the action of the filter  $b(t)$  may be applied to either the reflectivity or to the family of dilated wavelets. This dual view of the action of filter  $b(t)$  is not purely aesthetic but, instead, is of a practical interest. Indeed, the  $[r(t) * b(t)]$  term in eq. (9a) is nothing but the seismic trace and this equation shows that the experimental WR is practically obtained by computing the CWT of the seismic trace. Conversely, when filter  $b(t)$  is applied to the wavelet family  $\mathcal{D}_a \xi(t)$  (eq. 9b), the resulting kernels  $\mathcal{D}_a \xi(t) * b(t)$  acting on the reflectivity no more constitute a family of wavelets with a constant shape, and more or less pronounced distortions of the WR are expected. In practice, eq. (9b) is more comparable to eq. (8b) and useful to understand the distortions due to the limited frequency bandwidth of the data. Finally, observe that the kernel family  $\mathcal{D}_a \xi(t) * b(t)$  is the CWT of the filter as written in eq. (9c).

The distortions produced in the WR are controlled by the precise form of the filter  $b(t)$  and then depend on the spectrum of the seismic data. For a general form of  $b(t)$ , the distortions of the ridge functions are expected to be complex and analytically intractable. We now give some hints to practically undistort, at least partly, the ridge functions. The following discussion is based on our previous work on wavelet theory applied to potential fields, and the interested reader could find detailed theoretical developments in, for example, Moreau *et al.* (1997, 1999) and Sailhac *et al.* (2009).

There are some instances where the distortions are mathematically tractable and may be eliminated if the filter  $b(t)$  is a convolutionally stable function, that is, it belongs to a family of functions such that convolving two member functions gives a third function of the same family. For instance, convolving two Gaussians gives another Gaussian. Assuming that both the filter and the analysing wavelet are derivatives—possibly fractional—of a Gaussian function, the kernels  $\mathcal{D}_a \xi(t) * b(t)$  will also be the derivative of a Gaussian and will constitute a family of dilated wavelets of constant shape (e.g. Sailhac *et al.* 2009). The distortions of the ridge functions produced by convolutionally stable filters summarize as a rescaling and a translation along the dilation axis (see eqs 30 and 31 in Moreau *et al.* 1999), and the experimental WR may be undistorted.

In this study, the filter  $b(t)$  is only approximately known and the distortions of the ridge functions must be empirically corrected as no analytical formula can be derived. To do so, we estimate the distortions from the ridge function of a Heaviside discontinuity when

a limited frequency content is considered. In that case, the ridge function is not a straight line with a flat slope, as it should be without distortion (Fig. 1a-3), but a more complex curve instead. The distortion due to  $b(t)$  can then be removed, as a first approximation, by normalizing the ridge functions with this curve which provides an empirical estimate of the correction to apply. Fig. 2(c) illustrates this procedure for the case of the window discontinuity already discussed. In this figure, the dilation range is separated in two domains to mimic the HR and VHR data sets discussed by Ker *et al.* (2010) and presented below in a dedicated section. The distorted WR is obtained by applying filters—one for each data set—to limit the frequency content of the ideal WR shown in Fig. 2(b). It may be observed that the global plan view appearance of the distorted WR (Fig. 2c-2) looks very similar to the ideal WR (Fig. 2b-2) with two clusters of ridges at small dilations, a complicated merging of the ridges at intermediate dilations and, finally, four ridges typical of an impulse discontinuity at large dilations. The corrected ridge functions are shown in Fig. 2(c-3).

## 2.4 Remarks

The results discussed in Section 2 show that the multiscale informations given by the CWT of an impedance profile obtained by *in situ* data (Fig. 2a) are retrieved in the WR constructed with the reflected seismic waves (Fig. 2b). Despite the distortions produced by the frequency cut-off of real data, a large amount of the multiscale information can be retrieved through an empirical correction of the ridge functions (Fig. 2c). From a general point of view, the ridge functions, including the location points of their traces in the  $(z, a)$  plane, contain all information necessary to characterize a discontinuity. This property comes from the fact that both the CWT and WR are redundant as the wavelet family is not orthogonal. Hence, a subset of the CWT (and WR) is sufficient to reconstruct the analysed signal. In particular, the ridge functions constitute such a subset and Mallat & Hwang (1992) showed that a signal may be reconstructed from its ridge functions.

From the point of view of this study, the ridge functions constitute a multiscale data set containing the information brought by the original signal, and they may be used to compress signals. The localization of the ridge functions preserve their assignment to a given discontinuity—that is, reflector—and they can be viewed as seismic multiscale attributes suitable for further analysis.

The next two sections present the application of the multiscale analysis, both CWT and WR, to a marine seismic data set joined with *in situ* measurements. The data have been acquired during the ERIG3D cruise (2008) offshore Nigeria (Fig. 1) which provided the opportunity to investigate the first 25 m of hemipelagic sediments with deep-towed HR and VHR seismic and *in situ* coring techniques in deep-water  $\approx 1700$  m (Ker *et al.* 2010). The frequency ranges of the HR and VHR seismic data are (220–1050 Hz) and (580–2200 Hz), respectively, allowing to span more than three octaves in the dilation range in the experimental WR. The  $z$  resolution along the reconstructed *in situ* impedance profile equals 5 cm and allows to explore small dilations in the CWT.

## 3 APPLICATION OF THE CWT TO *IN SITU* ACOUSTIC IMPEDANCE DATA

### 3.1 Description of the *in situ* data

In 2008, the ERIG3D cruise was conducted on the R/V *Pourquoi Pas?* in the eastern Niger delta. The aim of this joined project

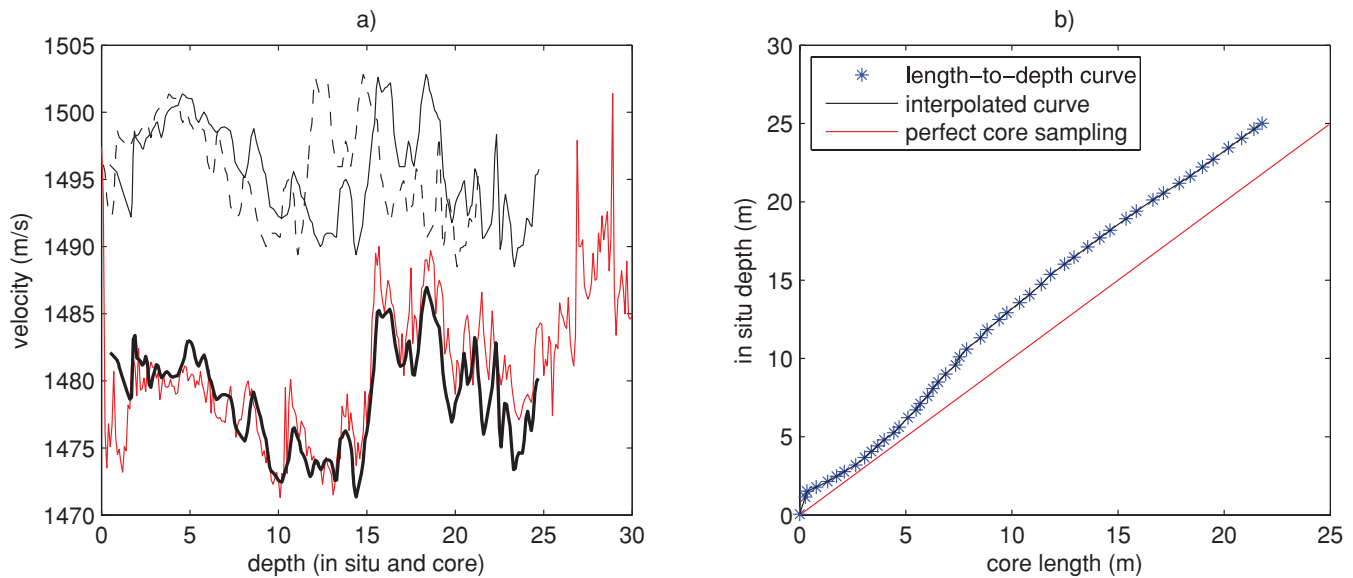


**Figure 3.** (a).  $P$ -wave velocity profiles: PENFELD *in situ* measurements (red), laboratory core measurements (dashed) + length-to-depth law correction (black) + environmental corrections (bold). (b) Length-to-depth relationship provided by the coring monitoring.

between IFREMER and the French oil company TOTAL was to assess the characterization of deep-water geohazards. During this cruise, ground truth data have been acquired at the VPS-05 site (Fig. 1a). *In situ* geotechnical measurements were performed with the PENFELD penetrometer developed by IFREMER (Sultan *et al.* 2007), to measure both cone penetration resistance and  $P$ -wave velocity down to 30 m below the seabed by steps of 2 cm (Fig. 1c). A core sample (CS-08), 22 m in length, was extracted on the same site with a Calypso piston corer (Kullenberg 1947) and direct lithological descriptions indicate that the sediments are mainly silty clay (Fig. 1b).

In addition, laboratory measurements were performed with a Geotek Multi Sensor core liner (Weaver & Schultheiss 1990) to obtain the bulk density and  $P$ -wave velocity logs along the CS-08 core. The bulk density was measured with a gamma ray attenuation method by steps of 1 cm. The  $P$ -wave measurements suffered from a lack of coupling between the sensor and the sediment, and were not satisfying. Instead, a non-conventional method involving the 500 kHz acoustic transducer of the PENFELD system was applied on CS-08 core for  $P$ -wave velocity measurements. The  $P$ -wave velocity profiles measured on the same superficial sediments at the laboratory and *in situ* (Fig. 3a, dashed and red lines, respectively) should be in good accordance. Actually, significant disagreements exist, leading in particular to a discrepancy along the  $z$ -axis because of core deformations. Because we aim at analysing the fine scale structure of the superficial sediments, density and  $P$ -wave velocity logs must correspond to real *in situ* conditions to compute the *in situ* acoustic impedance log. To do so, we define the corrections applied on the laboratory  $P$ -wave velocity log to fit the *in situ* measurements and then use the corrections to compensate the bulk density log available only from laboratory measurements.

### 3.2 *In situ* acoustic impedance log of the superficial sediments

Recent upgrades of the Calypso corer allow an improved sampling of the marine sediments together with a full monitoring of the

coring progression with accelerometers and pressure sensors (Bourillet *et al.* 2007). During the CS-08 coring, these control parameters indicate a penetration of about 25 m for a core length of 22 m only (Fig. 3b). This reveals an undersampling of the upper part of the sediment column, typical of core deformations during coring processes. We remove this artefact by applying the length-to-depth law defined from the coring monitoring (Salzat & Woerther 2010) and correct the  $z$ -axis of the laboratory  $P$ -wave velocity measurements along the core (black line in Fig. 3a). This original approach is based on physical parameters about the coring itself. It allows a control of the  $P$ -wave velocity deformation better than conventional methodologies based on correlation with the lithology derived from Cone Penetration Test measurements (Bourillet *et al.* 2007) or synchronization between synthetic seismic traces computed from core and seismic chirp data (Szérmétya *et al.* 2004; Manley & Brachfeld 2007).

Moreover, the laboratory  $P$ -wave velocities are roughly 1.5 per cent larger than the *in situ* measurements (Fig. 3a). This bias may be explained by environmental differences between the laboratory (20 °C and 0.1 MPa) and the deep-water conditions (4 °C and 17 MPa). The ratio method (Hamilton 1971) was used to correct the laboratory  $P$ -wave velocity measurements from temperature and hydrostatic pressure differences, leading to a very good agreement with the *in situ* velocity profiles validating the length-to-depth conversion law (Fig. 3a, thick and red lines, respectively).

The laboratory bulk density profile measured on CS-08 core suffered from the same deformation as the core  $P$ -wave velocity profile. We remove this artefact by using the length-to-depth conversion law applied to the  $z$ -axis of the velocity profile (Fig. 3b). Because near surface sediments were not sampled by the Calypso corer, the density values of the upper part of the profile were interpolated values. The environmental variations are negligible for the bulk density parameter (Hamilton 1971) and no corrections associated to temperature and depth have been applied on it.

From the corrected bulk density and *in situ*  $P$ -wave velocity profiles (Figs 4a and b), we establish the *in situ* acoustic impedance log of the superficial sediment down to 25 m under the seabed by steps of 5 cm (Fig. 4c). Note that the cross-plot presented in Fig. 4(d)

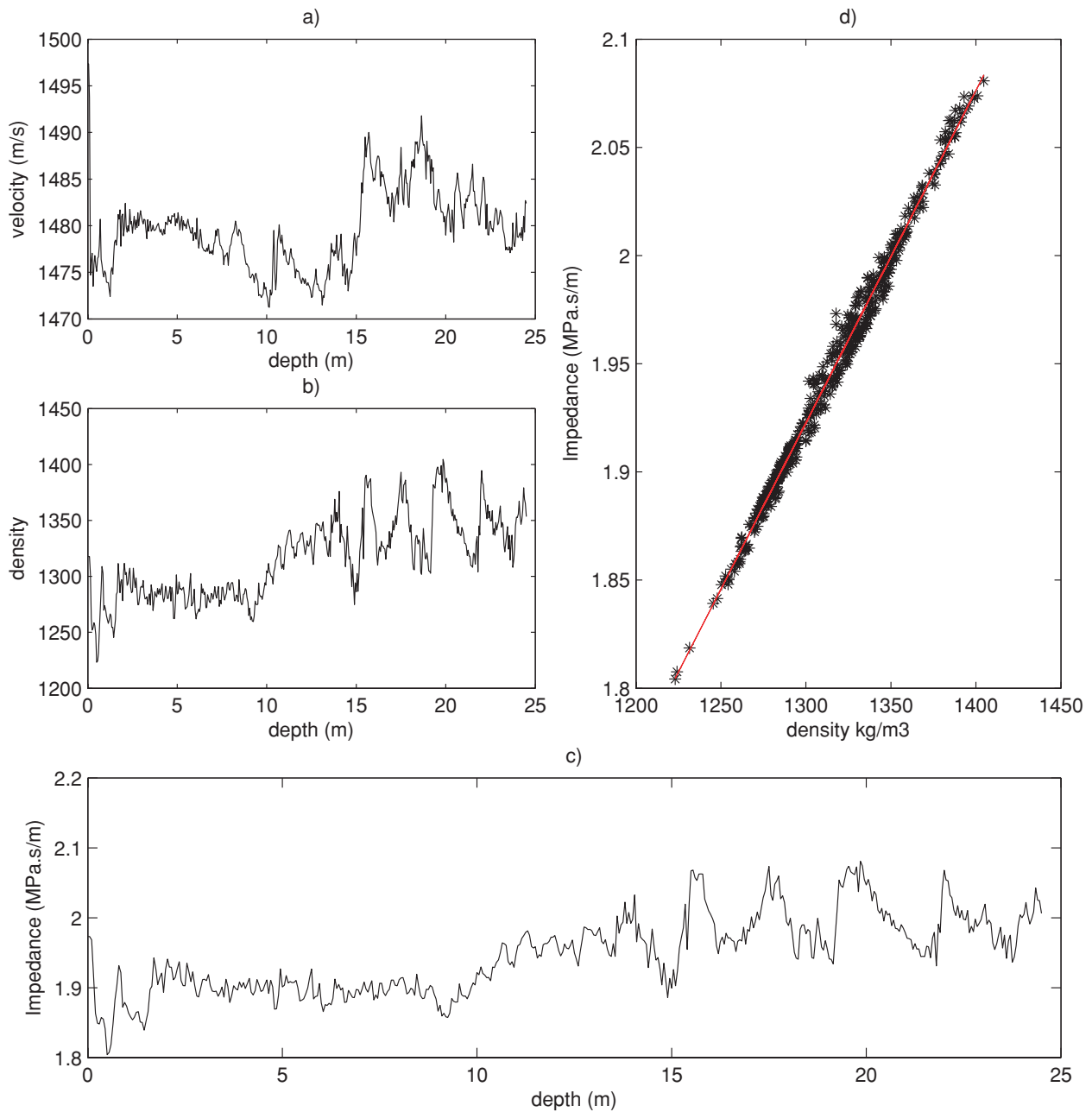


**Figure 4.** (a) *In situ* *P*-wave velocity log. (b) Corrected bulk density log. (c) Corrected acoustic impedance log. (d) Cross-plot acoustic impedance versus bulk density of the core sample.

shows that the acoustic impedance parameter is mainly controlled by the bulk density, that is, the *P*-wave velocity fluctuations have weak impacts on the seismic reflector strength.

### 3.3 CWT analysis of the acoustic impedance profile

We now apply the CWT analysis to the corrected acoustic impedance profile shown in Fig. 4(c). This profile appears very complex with conspicuous multiscale discontinuities. Qualitative descriptions based on direct observations of the sediment core show that the acoustic impedance is almost constant  $\sim 1.9 \text{ MPa s m}^{-1}$  down to a depth of 9 m before increasing up to  $\sim 1.95 \text{ MPa s m}^{-1}$  between 9 and 14 m. At greater depths, large scale oscillations of few metres in width occur in the  $1.9\text{--}2.07 \text{ MPa s m}^{-1}$  range.

The CWT of the impedance profile is shown in Fig. 5(b) for a dilation range corresponding to wavelengths from 0.25 to 3.75 m in accordance to the seismic data analysed in the next section. Several cone-like signatures are visible in the CWT map. These structures point towards the centres of discontinuities localized along the acoustic impedance log. The major signature typical of a Heaviside-like discontinuity centred at  $z = 0 \text{ m}$  is due to edge effects and does not deserve interpretation. Numerous intricate signatures of low amplitude are present in the  $0 < z < 15 \text{ m}$  range where the acoustic impedance display small-scale fluctuations. At greater depths  $z > 15 \text{ m}$ , several high-amplitude signatures with an internal structure showing cone coalescences at intermediate dilations as seen in the window example of Fig. 2. As demonstrated previously, this corresponds to transitions between global and internal structures of

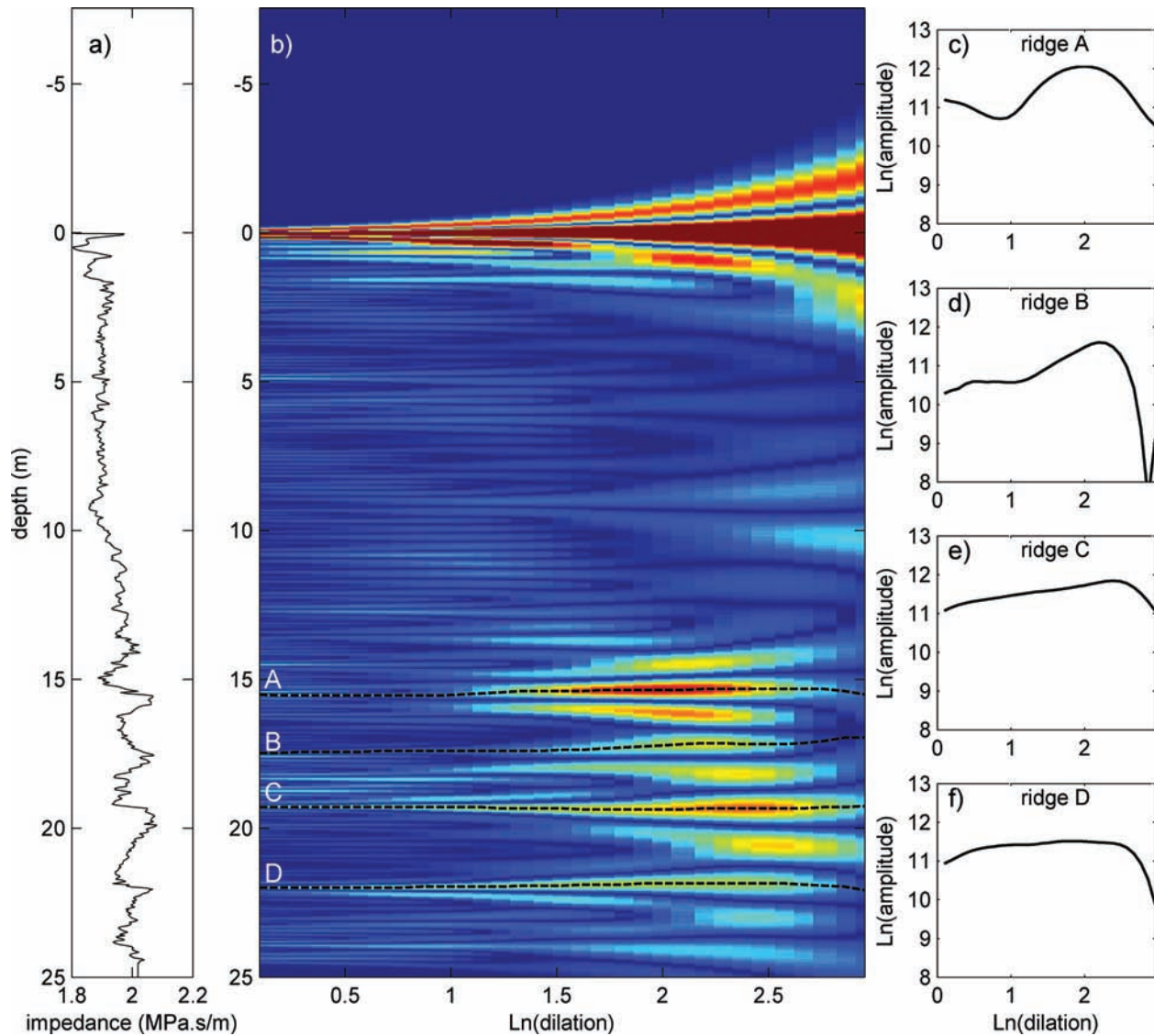


**Figure 5.** (a) Acoustic impedance log of the CS-08 core sample. (b) Modulus of the wavelet transform (WT) and selected ridge functions in dashed lines. (c, d, e and f) Ridge functions.

complex discontinuities. The core lithology analysis reveals that these complex structures correspond to silty layers of finite thickness.

We shall now discuss in more details the four signatures labelled *A*, *B*, *C* and *D* in Fig. 5(b) and, respectively located at  $z = 15.5$ ,  $17.5$ ,  $20$  and  $21.5$  m. The impedance discontinuities corresponding to these signatures are expected to produce strong seismic reflections in the seismic traces analysed in the next section. Selected ridge functions extracted from these signatures and corrected as explained in Section 2.3 are shown in Figs 5(c)–(f). Ridge *A* (Fig. 5c) is very similar to the ridge of the window discontinuity (Fig. 2) with a slope  $\alpha \simeq -1$  at large dilations and  $\alpha \simeq 0$  in the small-dilation range. A maximum is present at a characteristic dilation  $\ln(a_c) \simeq 2$  given a typical size  $\Delta z = a_c \lambda_0 / 2.61 \simeq 74$  cm (here  $\lambda_0 = 0.26$  m stands for the reference wavelength of the wavelet transform). A similar interpretation for ridge function *B* where  $\ln(a_c) \simeq 2.28$  gives  $\Delta z \simeq 98$  cm. The error in the thickness values is  $\pm 1$  cm. Ridges *C* and *D* are almost linear over the whole dilation range with a slope  $\alpha \simeq 0$  and correspond to step-like discontinuities.

#### 4 APPLICATION OF THE WR TO DEEP-WATER HR AND VHR SEISMIC DATA

##### 4.1 Presentation of the deep-water seismic data

In conjunction to ground truth data, deep-towed SYSIF seismic data have been acquired during the ERIG3D cruise. The SYSIF seismic survey crosses a submarine landslide, and the reader is referred to Ker *et al.* (2010) for a full presentation of the ERIG3D experiment and the processing of SYSIF seismic data.

The SYSIF deep-towed seismic device is equipped with acoustic sources covering the HR and VHR frequency bands— $220 < f < 1050$  Hz and  $580 < f < 2200$  Hz—allowing to image the subbottom with a metric (HR) to submetric (VHR) resolution for a depth penetration reaching 350 m in a silty clay sediment type. The SYSIF device acquires single channel data with a distance of 10 m between the seismic source and the receiver towed at a minimum altitude of 60 m above the seafloor (Table 1). These acquisition conditions correspond to an incident angle smaller than  $5^\circ$  and associated with

**Table 1.** Geophysical tools used during the ERIG3D cruise and acquisition parameters.

Seismic device	Frequency/duration (Hz)/(ms)	Altitude (m)	Shooting rate (s)	Ship speed (Kn)	SL (dB $\mu$ Pa@1 m)	Line name
VHR Sysif	[580–2200]/50	60	3	2	196	SY05-VHR-Pr01
HR Sysif	[220–1050]/100	150	3	2	196	SY06-HR-Pr01

altitudes much larger than the far field distance of the seismic source (12 m).

The SYSIF seismic profiles used in this study crosses the CS-08 core site (Fig. 1a). However, the acquisition of the HR and the VHR seismic profiles (Table 1), which involved both seismic source of the deep-towed SYSIF device, were not exactly at the same positions, except at the core site. As a consequence of this measurement uncertainty, only the HR component was considered in the assessment of complex reflectors over the submarine landslide. See Fig. 9(a) for an illustration of the HR SYSIF seismic profile.

#### 4.2 WR analysis of the seismic data near the CS-08 core site

We first present and discuss the WR of the SYSIF seismic trace nearest to the CS-08 core site, that is, the middle trace in Figs 6(a) and (d) for the HR and VHR frequency bands, respectively. The WR is obtained by using eq. (9a) which, in practice, is to compute the

CWT of the seismic trace with the  $\xi$  analysing wavelet. The resulting WRs are shown in Fig. 8(a) for the VHR band and in Fig. 8(b) for the HR band. The WR looks very similar to the CWT of the acoustic impedance profile (Fig. 5b), with a shallow strong conical signature followed by a low-amplitude region for  $2210 < t < 2230$  ms and strong-amplitude signatures for  $t > 2230$  ms. These late strong signatures visible in the WR are easily associated with those identified in the CWT of the acoustic impedance profile, and corrected ridge functions are shown in Figs 8(c)–(f), allowing quantitative comparisons with their impedance counterparts of Figs 5(c)–(f).

The WR ridges labelled *A* and *B* (Figs 8c and d) have a global appearance similar to their corresponding CWT impedance ridges of Figs 5(c) and (d) and are typical of the signature of a window discontinuity (Fig. 2c). These *A* and *B* WR ridges have a maximum at  $\ln(a_c) \simeq 2.1$  and  $\ln(a_c) \simeq 2.3$ , respectively, and using the relation  $\Delta z \simeq a_c \lambda_0 / 5.22$ , where  $\lambda_0 \simeq 0.52$  m is the reference wavelength of the wavelet, the corresponding window sizes are  $\Delta z \simeq 81$  cm for *A* and  $\Delta z \simeq 99$  cm for *B*. Here, we consider a constant *P*-wave velocity  $V = 1485 \text{ m s}^{-1}$ , that is, the impedance profile is mainly

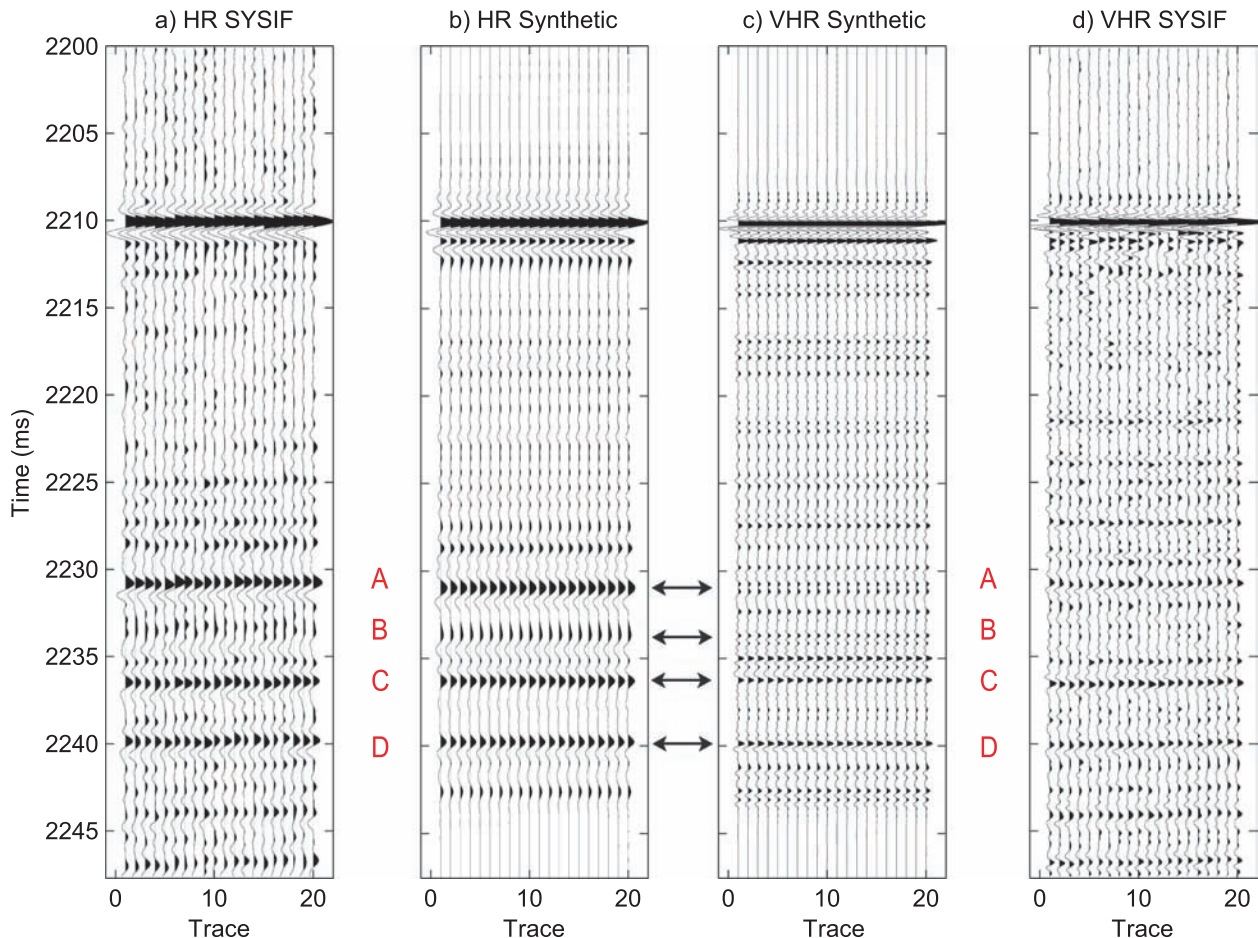


**Figure 6.** (a and b) Measured and synthetic HR seismic traces, respectively (220–1050 Hz). (c and d) Synthetic and measured VHR seismic traces, respectively (580–2200 Hz).

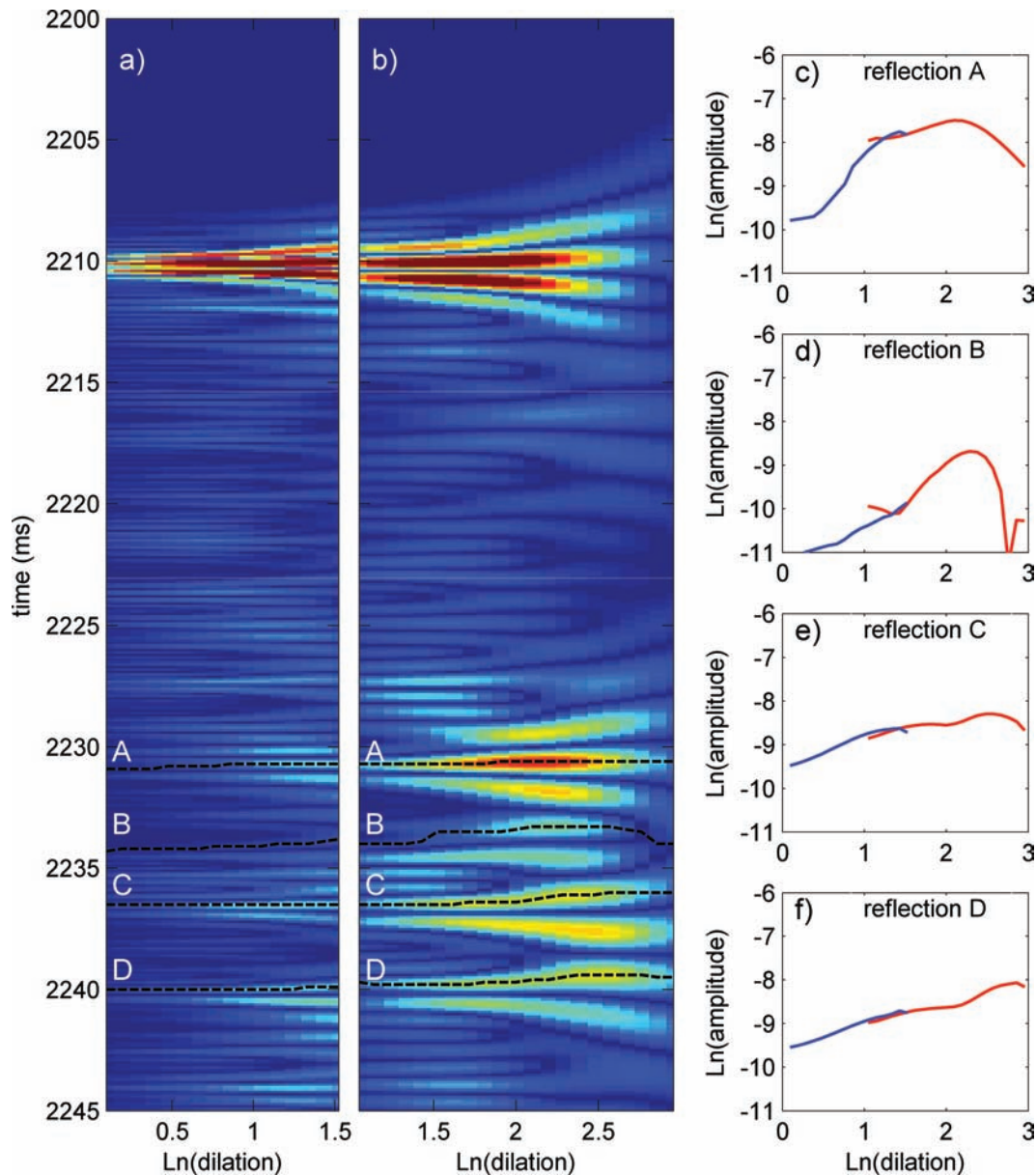


**Figure 7.** (a and b) Modulus of the wavelet transforms (WT) of the deep-towed seismic trace in the VHR (580–2200 Hz) and HR (220–1050 Hz) domains, respectively, and selected ridge functions in dashed lines. (c, d, e and f) Compensated ridge functions, in the VHR (blue) and HR (red) domains.

dominated by the density parameter.  $V$  is used to define the reference wavelength  $\lambda_0 = V/f_0$ , and if sharp velocity contrasts exist, the velocity inside the layer is considered. In the case of the WR of the window function, the uncertainty  $\delta e$  on the thickness  $\Delta z$  depends on  $\delta a$  and  $\delta V$ , which are associated to uncertainties on the  $a_c$  position and on the  $P$ -wave velocity  $V$ , respectively,  $\delta e = (a\delta V + V\delta a)/(2 \times 2.61f_0) \simeq V\delta a/5.22f_0$ . The uncertainty  $\delta e$  in the thickness values is  $\pm 2$  cm for reflectors  $A$  and  $B$ . These thickness values fall near the  $\Delta z \simeq 74$  cm and  $\Delta z \simeq 98$  cm values obtained from the  $A$  and  $B$  CWT ridges of the impedance profile. The WR ridges labelled  $C$  and  $D$  (Figs 8e and f) are almost linear over the whole dilation range as observed for the CWT impedance ridges of Figs 5(e) and (f). This signature is typical of homogeneous discontinuities without any particular scale.

The positive trends of the  $C$  and  $D$  WR ridges (Figs 8e and f) are clearly steeper than the trends of their companion CWT impedance

ridges and, although less conspicuous, this bias is also visible in the  $A$  and  $B$  ridges (Figs 8c and d). To understand this fact, we computed the synthetic WR corresponding to the impedance profile (Fig. 4c). The synthetic HR and VHR seismic traces are shown on Figs 6(b) and (c) and were obtained with the Goupillaud's method also used to compute the synthetic WR discussed in Section 2 (Fig. 2c). The WR corresponding to the HR and VHR synthetic traces are shown in Fig. 7 together with the ridge functions equivalent to the  $A$ ,  $B$ ,  $C$  and  $D$  ridges already discussed. We observe that these synthetic WR ridges do not display the positive trend presented in the WR ridges and are more similar to the ridges extracted from the CWT of the impedance profile. This indicates that the trend bias observed in the WR ridges of the SYSIF data do not result from the ridge correction procedure but, instead, are likely to be due to frequency-dependant attenuation, a phenomenon not considered in the modelling.

Seismic attenuation (Wang 2009), defined by the parameter  $\beta$  which can depend on the frequency  $f$ , can be expressed as

$$A_z = A_{z_0} \exp[-\beta(f)z], \quad (10)$$

where  $A_z$  and  $A_0$  are the wavefield amplitudes at depth  $z$  and at a reference depth  $z_0$ , respectively. Regarding the decrease of the seismic data ridge functions with frequency, we can assume an attenuation coefficient  $\beta$  which depends linearly on the frequency (Hamilton 1972; Harris *et al.* 1997), although several papers suggest a power law between  $\beta$  and  $f$  (Best *et al.* 2001 and Wang 2009 for a review). In our case, the attenuation coefficient is  $\beta \simeq 0.14 \text{ dB}/\lambda$ , corresponding to a quality factor  $Q \approx 200$  in accordance with the upper part of the  $Q$  range (30–180) measured for very fine silt and clay sediments (Shumway 1960; Hamilton 1972; Stevenson *et al.* 2002).

The  $\Delta z$  estimated from the WR ridges *A* and *B* (Figs 8c and d) correspond to a better spatial resolution than the extreme wavelengths

of the HR bandwidth, and the WR analysis then allows to perform some kind of super-resolution analysis. When this type of approach is possible, this is always at the expense of some additional information. Here, this information is brought by the assumption that the window model is valid so that the dilation  $a_c$  may be converted to an equivalent size  $\Delta z$ . The interest of the WR is that it enables to locally check the validity of the window model by looking at the shape of the ridge functions.

#### 4.3 WR analysis of the seismic data set

We now extend the WR analysis to the SYSIF data set shown on Fig. 9(a) which counts 1114 traces, 3 m apart, for a total length of 3340 m. We focus on the analysis of the reflectors *A* and *B* defined in the preceding section. These reflectors have WR ridge functions typical of window discontinuities with a maximum located at dilation  $a_c$  defining a characteristic size  $\Delta z$ .

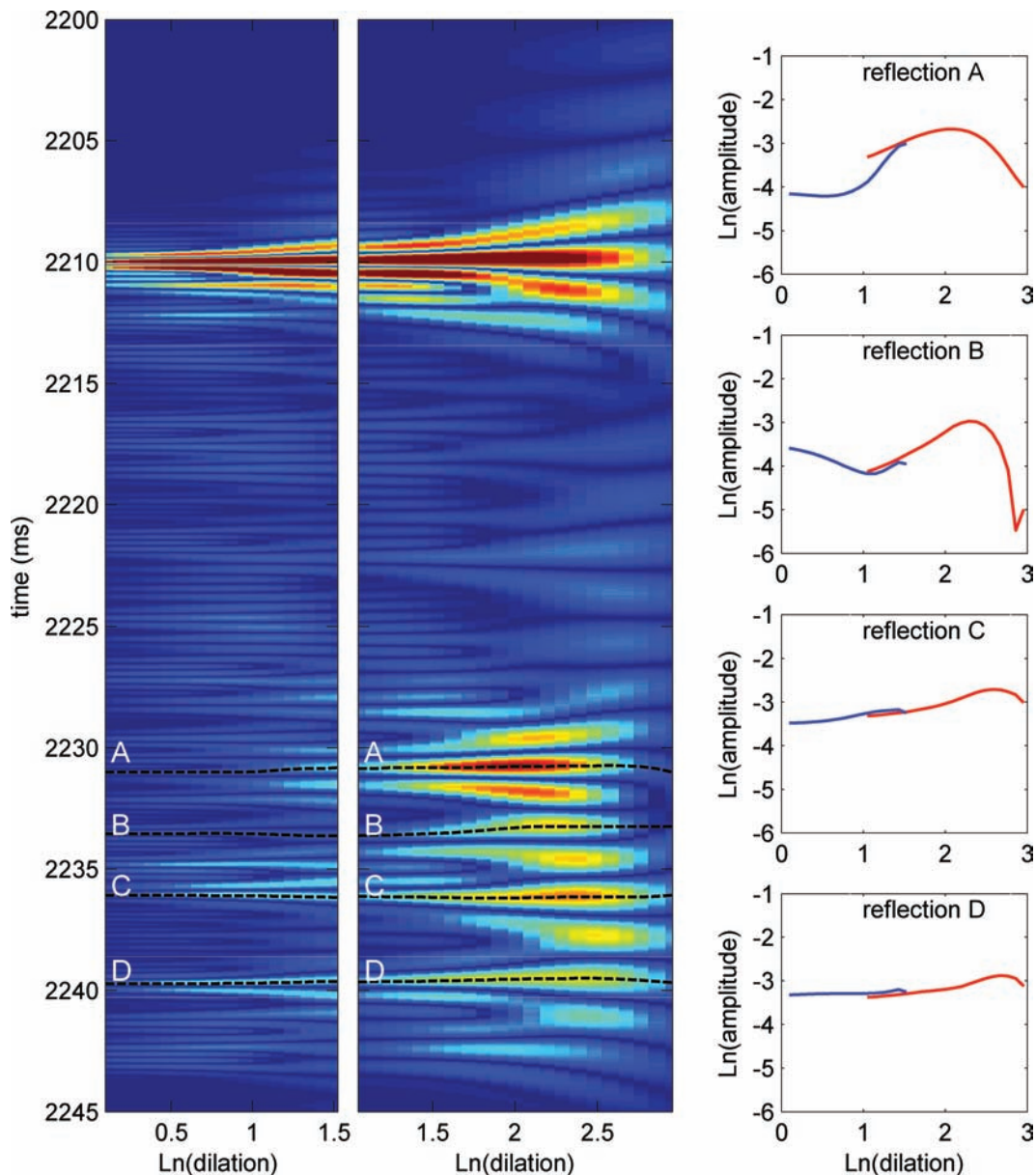


**Figure 8.** (a and b) Modulus of the synthetic wavelet responses (WR) including band-limited frequency of the seismic source in the VHR (580–2200 Hz) and HR (220–1050 Hz) domains, respectively, and selected ridge functions. (c, d, e and f) Compensated ridge functions, in the VHR (blue) and HR (red) domains.

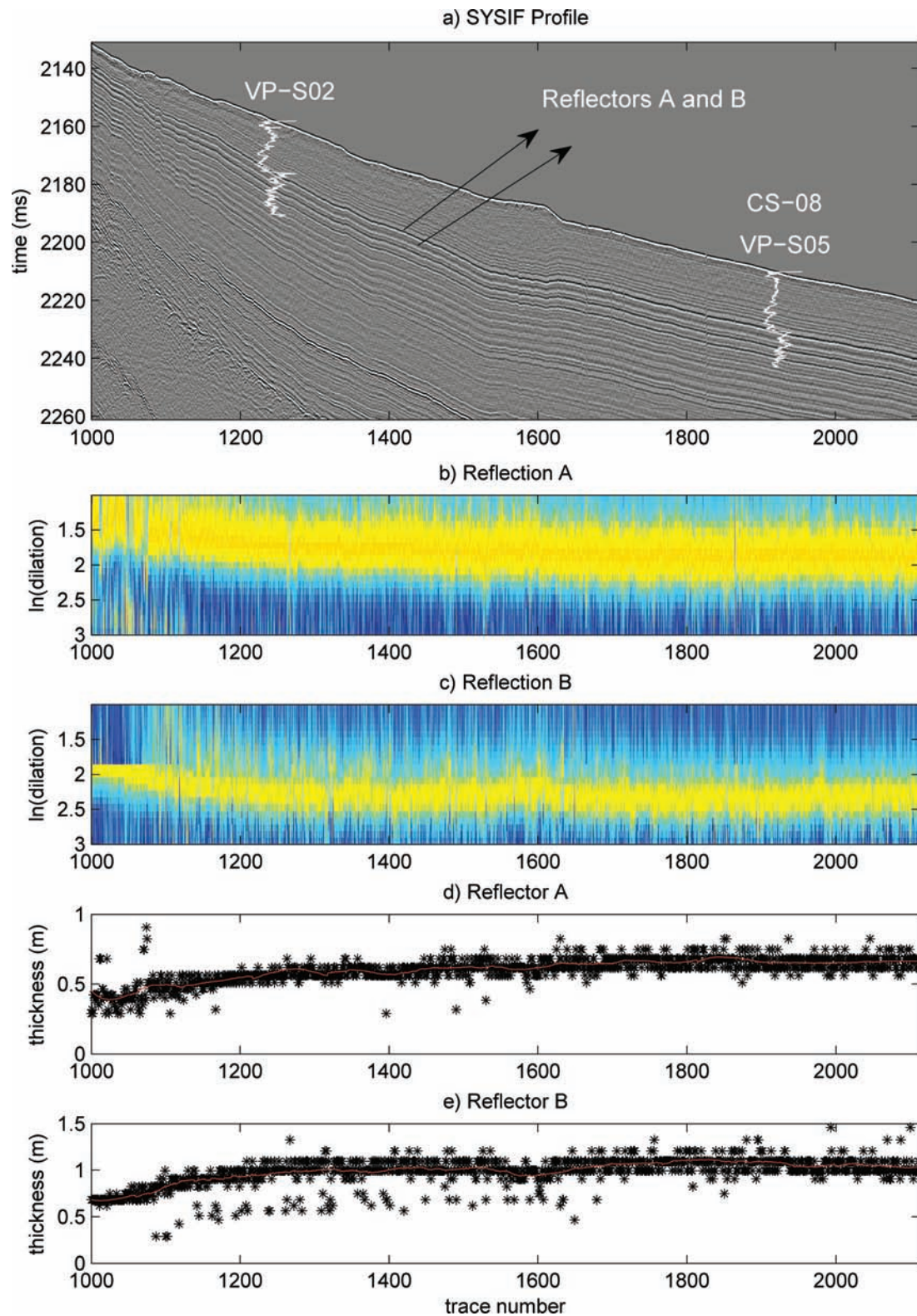


**Figure 9.** (a) Seismic profile across a submarine landslide in HR (220–1050 Hz) domain, *in situ* *P*-wave velocity profiles (VP-S02 and VP-S05), CS-08 core sample location and *A* and *B* seismic reflectors pointed with black arrows. (b and c) Ridge function attributes of reflectors *A* and *B*, respectively, as a function of the seismic trace number. (d and e) Reflector thicknesses extracted from the ridge function attributes. Note that both thicknesses increase from the upper part to the base of the landslide with a super-resolution.

Using the same approach as described in the preceding section, we performed a WR analysis of each trace and extracted the ridge functions related to reflectors *A* and *B*. These ridge functions are plotted versus the seismic trace number in Figs 9(b) and (c) where the maximum values appear in yellow and are centred on dilation  $a_c$ . The coherency between the ridge functions extracted from the remote seismic profile enables us to extend the calibration of trace 1923 relying on the *in situ* observations over a distance of more than 3000 m. The coherency of both ridges disappears at almost the same limit (traces 1000–1050) where the loss of reflectors continuity may be related to the presence of numerous faults. In addition, the reflector *A* may be affected by the submarine landslide (located from traces 1000 to 1634) as this reflector seems to constitute the base of the slide in its upper part (Sultan *et al.* 2007b).

A gentle and regular variation of dilation  $a_c$  is visible for both reflectors, indicating a progressive change of the characteristic size  $\Delta z$  whose value is reported on parts (d) and (e) of Fig. 9. The weaker amplitude of reflector *B* induces a poor signal-to-noise ratio for several traces in the first part of the profile where the  $\Delta z$  were discarded. On the overall, a clear increase of  $\Delta z$  is observed, for both reflectors, from the shallower to the deeper part of the seismic section, with  $\Delta z = 45 \pm 1 \rightarrow 80 \pm 2$  cm for reflector *A* and  $\Delta z = 55 \pm 1 \rightarrow 110 \pm 3$  cm for reflector *B*. Unfortunately, no other core sample is available to verify these thickness changes. Nevertheless, a second *P*-wave velocity profile (VP-S02) was measured close to trace number 1233, in the upper part of the landslide (Fig. 9a), and was used to confirm the identifications and depths of reflectors *A* and *B*. Actually, we observed similar *P*-wave velocity profiles on VP-S05 and VP-S02 where the geological reflectors are identified with the existence of velocity peaks in accordance with the reflector positions defined from the seismic survey. The variation of the thickness  $\Delta z$  is in accordance with growth strata associated with a fold characterized by a limb rotation and a tectonic uplift faster than the sediment filling (Shaw *et al.* 2004; Mercier *et al.* 2007). Thus, these thickness estimations can be used to quantify the kinematic evolution of this compressional anticline.

Let us again point out the fact that the reflector thicknesses determined with the WR ridges fall below the resolution of the SYSIF seismic profile used here, indicating that the seismic attributes constituted by the ridges allow to obtain information about the internal structure of the complex reflectors. As a first approximation, the reflectors appear as step-like interfaces in the seismic profile but are in fact complex discontinuities with characteristic sizes. The multiscale analysis, performed on an extended seismic profile, puts in evidence weak fluctuations of the thickness in good agreement with discrete ground truth data.

## 5 CONCLUDING REMARKS

In this paper, we presented a wavelet-based method to characterize acoustic impedance discontinuities present underground from a multiscale analysis of the reflected waves. The method, called the WR, extends the classical CWT of signals to the case of seismic waves.

As demonstrated by Le Gonidec *et al.* (2002, 2003) and recalled in this study, both the CWT and the WR are equivalent provided the Born approximation is valid and accounting for the propagation operator effects by an appropriate choice of the analysing wavelets. Such an approach is similar to the one described for potential fields and the Poisson wavelets semi-group where source singularities are detected and characterized through

the wavelet analysis of the potential field anomaly they produce (Moreau *et al.* 1997, 1999; Sailhac *et al.* 2009). We further show that, as first quoted by Mallat & Hwang (1992) in the case of the CWT, the relevant information concerning impedance discontinuities is contained in the ridge functions forming a subset of points in the WR map. By this way, ridges are information packets localized in the space–time domain and may be considered as a class of seismic attributes.

The theoretical developments and synthetic examples presented in Section 2 are applied to deep-water HR and VHR seismic data. The availability of *in situ* measurements allows to validate the relationship between CWT and WR, and to estimate the effects of the attenuation of seismic waves. Once validated, the method is applied to the whole seismic data set, and profiles of WR seismic attributes are constructed for two particular reflectors whose characteristic thickness is determined along the profile. This thickness falls below the resolution limit imposed by the shorter wavelength available in the seismic data, making the WR seismic attributes a super-resolution method. This is, of course, possible only by providing additional information which consists in choosing a particular class of discontinuity topology, that is, a window-like discontinuity in the present instance. However, this choice may be guided by the shape of the ridge functions themselves and it is consequently possible to assign a particular discontinuity model to each reflector.

The HR and VHR seismic data used in this study span a particularly wide frequency bandwidth which enables to compute the WR over a wide dilation range. We hope that such high-quality deep-water data will be more frequent in a near future, making multiscale seismic attributes of a wider usage to perform a local analysis of seismic traces and to characterize the fine structure of reflectors.

## ACKNOWLEDGMENTS

This work benefited from the invaluable support of TOTAL colleagues Sylvie Grimaud and Jérôme Adamy. The field experiments were conducted with the help of Pierre Leon, Henri Martinossi, Sébastien Garziglia, Nabil Sultan and Michel Voisset from IFREMER. This is IGP contribution number 3214.

## REFERENCES

- Aki, K. & Chouet, B., 1975. Origin of Coda waves: source, attenuation, and scattering effects, *J. geophys. Res.*, **80**, 3322–3342, doi:10.1029/JB080i023p03322.
- Alexandrescu, M., Gibert, D., Hulot, G., Le Mouél, J.-L. & Saracco, G., 1995. Detection of geomagnetic jerks using wavelet analysis, *J. geophys. Res.*, **100**, 12 557–12 572.
- Banchs, R.E. & Michelena, R.J., 2002. From 3D seismic attributes to pseudo well-log volumes using neural networks: practical considerations, *Leading Edge*, **21**, 996–1001.
- Banik, N.C., Lerche, I. & Shuey, R.T., 1985. Stratigraphic filtering. Part 1: derivation of the O'Doherty-Anstey formula, *Geophysics*, **50**, 2768–2774.
- Barnes, A.E., 2001. Seismic attributes in your facies, *CSEG Recorder*, **26**, 41–47.
- Best, A.I., Huggett, Q.J. & Harris, A.J.K., 2001. Comparison of *in situ* and laboratory measurements on Lough Hyne marine sediments, *J. acoust. Soc. Am.*, **110**, 695–709, doi:10.1121/1.1382616.
- Bourillet, J.-F., Damy, G., Dussud, L., Sultan, N., Woerther, P. & Migeon, S., 2007. Behaviour of a piston corer from accelerometers and new insights on quality of the recovery, *Proceedings of the 6th International Offshore Site Investigation and Geotechnics Conference: Confronting New Challenges and Sharing Knowledge*, 2007 September 11–17, London.

- Burridge, B., Papanicolaou G. & White, B., 1988. One-dimensional wave propagation in a highly discontinuous medium, *Wave Motion*, **10**, 19–44.
- Castagna, J., Sun, S. & Siegfried, R.W., 2003. Instantaneous spectral analysis: detection of low-frequency shadows associated with hydrocarbons, *Leading Edge*, **22**, 120–127.
- Chopra, S., Castagna, J. & Portnaguine, O., 2006. Seismic resolution and thin-bed reflectivity inversion, *CSEG Recorder*, **31**, 19–25.
- Chopra, S. & Marfurt, K.J., 2008. Emerging and future trends in seismic attributes, *Leading Edge*, **27**, 298–318.
- Chung, H.-M. & Lawton, D.C., 1995. Amplitude responses of the thin beds: Sinusoidal approximation versus Ricker approximation, *Geophysics*, **60**, 223–230.
- Fomel, S., 2007. Local seismic attributes, *Geophysics*, **72**, A29–A33, doi:10.1190/1.2437573.
- Frankel, A. & Clayton, R.W., 1986. Finite difference simulations of seismic scattering implications for the propagation of short-period seismic waves in the crust and models of crustal heterogeneity, *J. geophys. Res.*, **91**, 6465–6489.
- Gastaldi, C., Biguenet, J.-P. & De Pazzis, L., 1997. Reservoir characterization from seismic attributes: An example from the Peciko Field (Indonesia), *Leading Edge*, **16**, 263–266.
- Gesret, A., Laigle, M., Diaz, J., Sachpazi M. & Hirn, A., 2010. The oceanic nature of the African slab subducted under Peloponnesus: thin-layer resolution from multiscale analysis of teleseismic P-to-S converted waves, *Geophys. J. Int.*, **183**, 833–849.
- Gettrust, J.F., Ross, J.H. & Rowe, M.M., 1991. Development of a low frequency deep-tow geoacoustics system, *Sea Technol.*, **32**, 23–32.
- Goupillaud, P., 1961. An approach to inverse filtering of near-surface layer effects from seismic records, *Geophysics*, **26**, 754–760.
- Goupillaud, P., Grossmann, A. & Morlet, J., 1984. Cycle-octave and related transforms in seismic signal analysis, *Geoexploration*, **23**, 85–102.
- Gray, S.H. & Bleistein, N., 1986. Imaging and inversion of zero-offset seismic data, *Proc. IEEE*, **74**, 440–456.
- Grossman, A., Holschneider, M., Kronald, R.M. & Morlet, J., 1987. Detection of abrupt changes in sound signals with the help of wavelet transform, in *Inverse Problems. An Interdisciplinary Study: Advances in Electronics and Electron Physics*, Supp., 19, pp. 298–306, Academic Press, San Diego, CA.
- Hamilton, E.L., 1971. Prediction of in-situ acoustic and elastic properties of marine sediments, *Geophysics*, **36**, 266–284.
- Hamilton, E.L., 1972. Compressional-wave attenuation in Marine Sediments, *Geophysics*, **37**, 266–284.
- Harris, P.E., Kerner, C. & White R.E., 1997. Multichannel estimation of frequency dependant Q from VSP data, *Geophys. Prospect.*, **45**, 87–109.
- Holschneider, M., 1988. On the wavelet transformation of fractal objects, *J. Stat. Phys.*, **50**, 953–993.
- Holschneider, M., 1995. *Wavelets: An Analysis Tool*, Clarendon, Oxford, 423pp.
- Kallweit, R.S. & Wood, L.C., 1982. The limits of resolution of zero-phase wavelets, *Geophysics*, **47**, 1035–1046.
- Ker, S., Le Gall, Y., Marsset, T. & Leon, P., 2008. SYSIF, a low frequency seismic profiler for near-bottom marine geophysics, in *Proceedings of the 70th EAGE Conference and Exhibition*, Rome.
- Ker, S., Marsset, B., Garziglia, S., Le Gonidec, Y., Gibert, D., Voisset M. & Adamy, J., 2010. High-resolution seismic imaging in deep sea from a joint deep-towed/OBH reflection experiment: application to a Mass Transport Complex offshore Nigeria, *Geophys. J. Int.*, **182**, 1524–1542.
- Kullenberg, B., 1947. The piston core sampler, *Sven. Hydrogr. Biol. Komm. Skr. Ny Ser. Hydrogr.*, **3**, 1–46.
- Le Gonidec, Y. & Gibert, D., 2006. The wavelet response as a multiscale characterization of scattering processes at granular interfaces, *Ultrasonics*, **44**, 381–390.
- Le Gonidec, Y. & Gibert, D., 2007. Multiscale analysis of waves reflected by granular media: acoustic experiments on glass beads and effective medium theories, *J. geophys. Res.*, **112**(B05103), doi:10.1029/2006JB004518.
- Le Gonidec, Y., Gibert, D. & Proust, J.-N., 2002. Multiscale analysis of waves reflected by complex interfaces: basic principles and experiments, *J. geophys. Res.*, **107**(B9), 2184, doi:10.1029/2001JB000558.
- Le Gonidec, Y., Conil, F. & Gibert, D., 2003. The wavelet response as a multiscale NDT method, *Ultrasonics*, **41**, 487–497.
- Mallat, S., 1998, *A Wavelet Tour of Signal Processing*, 2nd edn, Academic Press Inc., Salt Lake City, UT.
- Mallat, S. & Hwang W.L., 1992. Singularity detection and processing with wavelets, *IEEE Trans. Inf. Theory*, **38**, 617–643.
- Manley, P.L. & Brachfeld, S., 2007. Synthetic seismograms and spectral cycles on the Andvord and Schollaert Drifts: Antarctic Peninsula: a keystone in a changing world in *Online Proceedings of the 10th ISAES*, eds Cooper A.K., Raymond C.R. et al., USGS Open-file Report 2007–1047, Short Research 018, 5p; doi:10.3133/of2007-1047.srp018.
- Marsset, T., Marsset, B., Ker, S., Thomas, Y. & Le Gall, Y., 2010. High and very high resolution deep-towed seismic system: performance and examples from deepwater Geohazard studies, *Deep-Sea Res.*, **57**, doi:10.1016/j.dsr.2010.01.001.
- Mercier, E., Rafini, S. & Ahmadi R., 2007. Folds kinematics in “Fold-and-Thrust Belts” the “Hinge Migration” question, a review, in *Thrust Belts and Foreland Basins, Frontiers in Earth Sciences, Part IV*, 135–147, Springer, Berlin, doi:10.1007/978-3-540-69426-7-7.
- Moreau, F., Gibert, D., Holschneider, M. & Saracco, G., 1997. Wavelet analysis of potential fields, *Inv. Problems*, **13**, 165–178.
- Moreau F., Gibert, D., Holschneider, M. & Saracco, G., 1999. Identification of sources of potential fields with the continuous wavelet transform: basic theory, *J. geophys. Res.*, **104**, 5003–5013.
- Morlet, J., Arens, G., Fourgeau, E. & Glard, D., 1982. Wave propagation and sampling theory, part I: complex signal and scattering in multilayered media, *Geophysics*, **47**, 203, doi:10.1190/1.1441328.
- Parkes, G. & Hatton, L., 1986. *The Marine Seismic Source*, Kluwer Academic Publishers, Dordrecht.
- Pennington, W.D., 2001. Reservoir geophysics, *Geophysics*, **66**, 25–30.
- Pujol, J. & Smithson, S.B., 1991. Seismic wave attenuation in volcanic rocks from VSP experiments, *Geophysics*, **56**, 1441–1455.
- Resnick, J.R., 1990. Stratigraphic filtering, *Pure appl. Geophysics*, **132**, 49–65, doi:10.1007/BF00874357.
- Sailhac, P., Gibert, D. & Boukerbout, H., 2009. The theory of the continuous wavelet transform in the interpretation of potential fields: a review, *Geophys. Prospect.*, **57**, 517–525, doi:10.1111/j.1365.2478.2009.00794.x.
- Salzat, L. & Woerther, P., 2010. Géométrie et qualité des couches par carottage gravitaire à piston, report, Ifremer, Brest.
- Shaw, J.H., Novoa, E. & Connors, C.D., 2004. Structural controls on growth stratigraphy in contractional fault-related folds, *AAPG Memoir*, **82**, 400–412.
- Sheng, P., Zhang, Z.Q., White, B. & Papanicolaou, G., 1986. Multiple-scattering noise in one dimension: universality through localization-length scaling, *Phys. Rev. Lett.*, **57**, 1000–1003.
- Sheriff, R.E., 1991. *Encyclopedic Dictionary of Exploration Geophysics*, Society of Exploration Geophysicists, Tulsa, OK, 376pp.
- Sheriff, R.E., 1992. *Reservoir Geophysics*, Society of Exploration Geophysicists, Tulsa, OK.
- Shumway, G., 1960. Sound speed and absorption studies of marine sediments by a resonance method, *Geophysics*, **25**, 451–467.
- Stevenson, I.R., McCann, C. & Runciman, P.B., 2002. An attenuation-based sediment classification technique using Chirp sub-bottom profiler data and laboratory acoustic analysis, *Mar. Geophys. Res.*, **23**, 277–298.
- Strecker, U. & Uden, R., 2002. Data mining of 3D poststack seismic attribute volumes using Kohonen self-organizing maps, *Leading Edge*, **21**, 1032–1037.
- Sultan, N., Voisset, M., Marsset, B., Marsset, T., Cauquil, E. & Colliat, J.L., 2007b. Potential role of compressional structures in generating submarine slope failures in the Niger Delta, *Mar. Geol.*, **237**, 169–190.
- Sultan, N., Voisset, M., Marsset, T., Vernant, A.M., Cauquil, E., Colliat, J.L. & Curinier, V., 2007a. Detection of free gas and gas hydrate based on 3D seismic data and cone penetration testing: an example from the Nigerian Continental Slope, *Mar. Geol.*, **240**(1–4), 235–255.
- Széréméta, N., Bassinot, F., Balut, Y., Labeyrie, L. & Pagel, M., 2004. Over-sampling of sedimentary series collected by giant piston corer: evidence

and corrections based on 3.5 kHz chirp profiles, *Paleoceanography*, **19**, PA1005, doi:10.1029/2002PA000795.

Wang, Y., 2009. *Seismic Inverse Q Filtering*, Blackwell Publishing, Oxford.  
 Weaver, P.P.E. & Schulteiss, P.J., 1990. Current methods for obtaining, logging and splitting marine sediments cores, *Mar. geophys. Res.*, **12**, 85–100.  
 Widess, M.A., 1973. How thin is a thin bed? *Geophysics*, **38**, 1176–1180.  
 Wood, W., Gettrust J.F. & Spychalski, S., 2003. A new deep-towed, multi-channel seismic system, *Sea Technol.*, **44**, 44–49.

## APPENDIX A: RIDGE FUNCTION OF A WINDOW DISCONTINUITY

In the framework of the wavelet transform, homogeneous discontinuities do not have any characteristic size, that is, their appearance remains unchanged whatever the scale considered (see eq. 3). For instance, the Dirac impulse function,  $\delta(z)$  and the Heaviside step function,  $H(z) = \int_{-\infty}^z \delta(\xi) d\xi$  are characterized by straight ridge functions all over the dilation range (Fig. A1). Moreover, the number  $N$  of ridge functions in the CWT, which depends on the homogeneity degree  $\alpha$  of the discontinuity, is  $N = 4$  and  $3$  for the  $\delta$  and  $H$  singularities, respectively.

A complex discontinuity has a characteristic size, such as the thickness  $\Delta z$  of the window function  $w(z)$ . The ridge functions of this discontinuity, constructed with two Heaviside functions (see eq. 4), possess a maximum value at the characteristic wavelength  $\lambda_c = a_c \lambda_0$  (see Section 2.1 for details). An analytical relation between  $a_c$  and  $\Delta z$  is not straightforward (Widess 1973), but Kallweit & Wood (1982) and Chung & Lawton (1995) report the following relationship, dealing with Ricker wavelets:  $\Delta z \simeq 1/2.61 \lambda_c$ . To go

further, we can write the wavelet transform of  $w$ , where  $w$  is defined in eq. (4), as two Heaviside discontinuities, as follows:

$$W[\psi, p](z, a) = \frac{1}{a} \psi\left(\frac{z}{a}\right) * w(z) = \psi_a(z) * w(z) \quad (\text{A1a})$$

$$= \psi_a^{(-1)}\left(z + \frac{\Delta z}{2}\right) - \psi_a^{(-1)}\left(z - \frac{\Delta z}{2}\right), \quad (\text{A1b})$$

where the exponent  $(-1)$  stands for the integration operation applied on  $\psi_a$ . Note that the centre of the discontinuity  $w(z)$  is at  $z = 0$ . For each dilation  $a$ , the maxima of eq. (A1b) compose the ridge functions and their positions  $z$  satisfy the relation

$$\psi_a\left(z + \frac{\Delta z}{2}\right) = \psi_a\left(z - \frac{\Delta z}{2}\right). \quad (\text{A2})$$

By considering  $\psi$  as the third derivative of a Gaussian function, we demonstrate that the positions  $z$  are solutions of the system

$$\begin{cases} P(z) = \left(z - \frac{\Delta z}{2}\right) \left[6 - \omega_a^2 \left(z - \frac{\Delta z}{2}\right)^2\right] e^{\omega_a^2 \frac{\Delta z}{4} z} \\ P(-z) = -P(z), \end{cases} \quad (\text{A3})$$

where  $\omega_a$  is defined by  $\omega_a = 2\pi/a$ , where we consider  $\lambda = 1$  m to work in the reduced wavelength framework. It is worth underlining that a solution at  $z = 0$ , that is,  $P(-z) = -P(z)(z = 0)$ , only exists when the dilation  $a$  equals a critical dilation  $a_{cr} = \frac{\pi}{\sqrt{6}} \Delta z$ . This means that the number  $N$  of ridge functions depends on  $a$ . Note that in the example of Fig. 2 presented in Section 2, the wavelength of the analysing wavelet is 0.26 m and  $a_{cr} = 2.96$  [ $\ln(a_{cr}) = 1.08$ ]

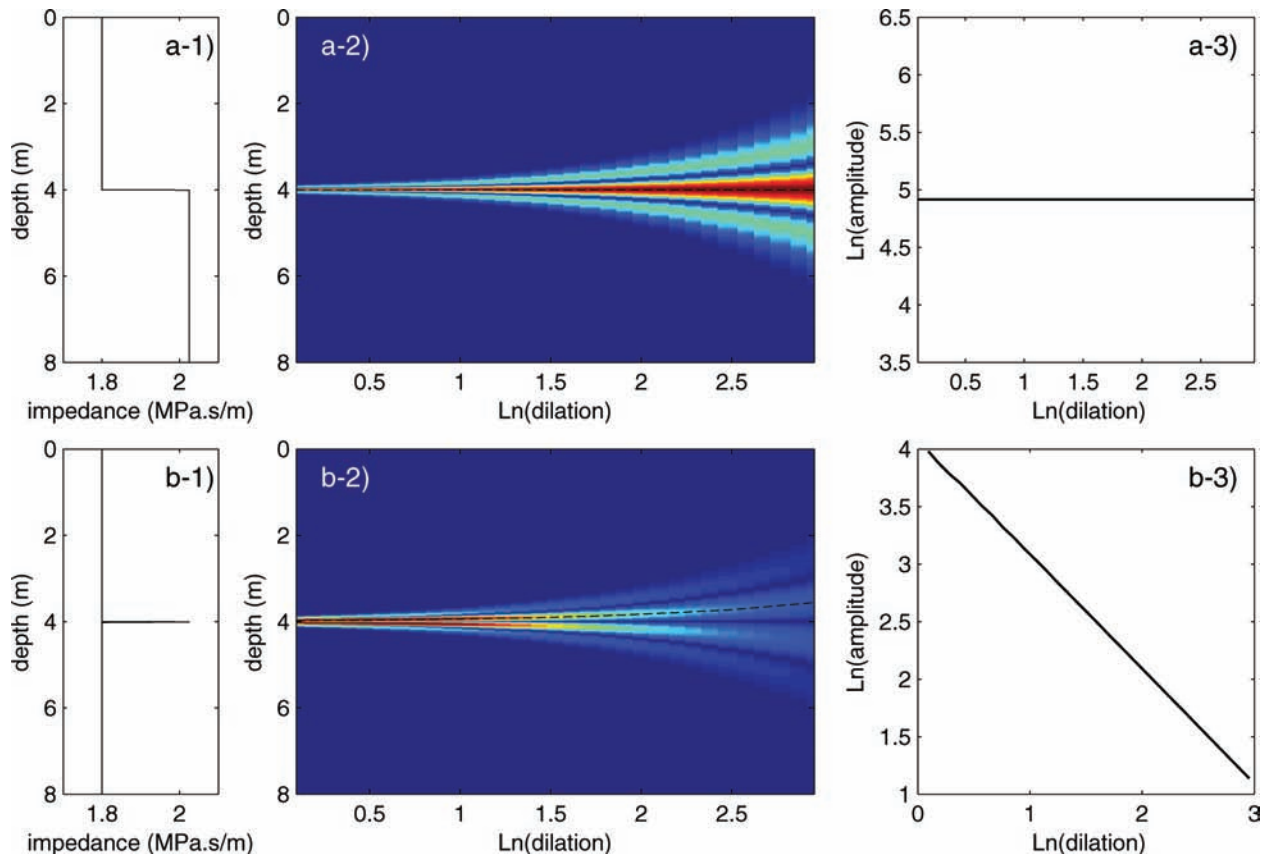


**Figure A1.** Top panels (left- to right-hand side): Heaviside step function, CWT modulus and ridge function. Bottom panels (left- to right-hand side): Dirac impulse function, CWT modulus and ridge function.

which is half the dilation  $a_c$  of the ridge function maximum defined in Section 2.1. At small dilations  $a < a_{cr}$ , solutions of eq. (A3) are the roots of  $P(z)(z > 0)$  and  $P(-z)(z < 0)$ . In this limit  $N = 6$  and  $w$  is equivalent to two distinctive Heaviside discontinuities, both characterized by three ridge functions:  $z_1 = -\frac{\Delta z}{2} - \frac{\sqrt{6}}{\omega_a}$ ,  $z_2 = -\frac{\Delta z}{2}$  and  $z_3 = -\frac{\Delta z}{2} + \frac{\sqrt{6}}{\omega_a}$  for the first Heaviside and  $z_4 = \frac{\Delta z}{2} - \frac{\sqrt{6}}{\omega_a}$ ,  $z_5 = \frac{\Delta z}{2}$  and  $z_6 = \frac{\Delta z}{2} + \frac{\sqrt{6}}{\omega_a}$  for the second Heaviside. Note that  $z_2$  and  $z_5$  do not depend on  $\omega_a$ , that is, they correspond to ridge functions centred on the edges of the discontinuity. At larger dilations, the number of ridge function is  $N = 5$  when  $a = a_{cr}$  where  $z_3 = z_4 = 0$ , and is then reduced to  $N = 4$  at dilations  $a > a_{cr}$  where the  $w$  discontinuity can be assimilated to a Dirac discontinuity.

## APPENDIX B: COMPUTATION OF SYNTHETIC WAVELET RESPONSES

In this work, we perform the Goupillaud's model (Goupillaud 1961) to compute the Green's function of a medium sounded in normal incidence by plane waves. This forward modelling is very effective for a 1-D structure which WR can be computed by convolving its

Green's function with the wavelet family. We consider a thickness  $\Delta z = 0.6$  m for the window discontinuity which apparent aperture is 1.2 m when sounded by wavelets of wavelength  $\lambda$ . The wavelet dilation is  $a = \lambda f_0 / c$ , where  $c = 1500 \text{ m s}^{-1}$  is the sound velocity and  $f_0 = 2860$  Hz the central frequency of the mother-analysing wavelet, which corresponds to  $\lambda_0 = 0.52$  m, that is, twice the reference wavelength of the wavelet transform analysis (see Section 2.1). The ridge function reaches a maximum value at the dilation  $a_c \simeq 6.05 [\ln(a_c) \simeq 1.8]$ , which leads to a characteristic wavelength  $\lambda_c \simeq 3.15$  m. This characteristic value is then related to the real width of the window function by  $\lambda_c \simeq 2\Delta z \times 2.61$  because of the two-way traveltime involved in the WR. These quantitative descriptions show that the ridge function analysis based on either the WR or the wavelet transform are in good accordance. Moreover, we observe that multiple scattering can be neglected and the Born approximation acceptable in this case, where the reflected wavefield of the window function in response to a Dirac source equals the reflectivity function (Gray & Bleisten 1986)

$$r(t) \equiv \frac{1}{2} \frac{d}{dt} \ln \gamma(t), \quad (\text{B1})$$

where  $\gamma(t)$  is the acoustic impedance of the medium.